CONF-781138--1

PROTON RADIOGRAPHY APPLICATION TO MEDICAL IMAGING

by

Stephen L. Kramer, D. Read Moffett, Roland L. Martin
Eugene P. Colton and V. William Steward

MASTER

Prepared for

64th Scientific Assembly and Annual Meeting
of the
Radiological Society of North America

Chicago, Illinois

November 25, 1978 - December 1, 1978

UofC-AUA-USDOE

ARGONNE NATIONAL LABORATORY, ARGONNE, ILLINOIS

Operated under Contract W-31-109-Eng-38 for the
U. S. DEPARTMENT OF ENERGY

Work-in-progress paper submitted to the 64th Scientific Assembly and Annual Meeting of the Radiological Society of North America, November 29, 1978.

PROTON RADIOGRAPHY APPLICATION TO MEDICAL IMAGING*

Stephen L. Kramer, Ph.D., D. Read Moffett, Ph.D., Ronald L. Martin, Ph.D., and Eugene P. Colton, Ph.D.
Argonne National Laboratory

V. William Steward, M.D.
University of Chicago

Abstract

In order to demonstrate the potential advantages of proton radiography for medical imaging, a 205 MeV proton radiography beam was developed using the Argonne National Laboratory Booster I synchrotron. Data were taken using a narrow scanning beam and an electronic detector system. The proton radiographs presented here demonstrate a significant dose reduction and improved mass resolution over conventional x-ray techniques. The radiographs also show significant differences in the proton stopping power of biological tissues and, therefore, considerable potential in soft tissue imaging. Also presented is the motivation for the interest in developing a proton tomographic scan system.

Introduction

Shortly after their discovery, x-rays were employed to image the human anatomy. Since those initial attempts, considerable improvement in the technology of x-ray imaging has taken place but the basic principles remain unchanged. Despite these changes, there still remain many problems in x-ray imaging, most important of which are the lack of sufficient mass resolution to image soft tissue structure and a high and widely variable radiation exposure to the patient.

*Work supported by the U.S. Department of Energy and the National Cancer Institute through Contract No. NO1-CB-43918.

Several years ago, it was suggested that charged particles could be employed for imaging purposes;[1-2] and although several attempts[3-6] to demonstrate the advantages of these techniques have been made, this technique continues to be viewed largely as a novel idea but without clinical applications. This attitude has mainly resulted from the difficulties and expense in providing a suitable source of particles but also from a lack of understanding of the behavior of charged particles and how they might be employed for medical imaging. In 1975, it was shown by Martin et al.[7] that a low intensity 200 MeV proton synchrotron could be built, using recently developed accelerator technology, to provide a beam for radiographic imaging at a cost competitive with the state-of-the-art x-ray systems. With this demonstration that the cost of providing a source for clinical proton radiography need not be prohibitive, we have undertaken a program to demonstrate further the potential advantages of proton radiography to medical imaging.

The basis for the interest in proton radiography can be easily seen from Fig. 1 where the transmission curve for 200 MeV protons (range 25.5 g/cm^2 of tissue) is compared to a 40 keV x-ray beam. The very rapid change of the proton transmission curve will yield much larger changes in the transmitted proton fluence (for a detector located at the rapid fall off of the curve) than for the x-ray fluence, as the result of a small change in the total mass of material in the beam. In a radiograph of a uniform object, the ability to detect a change in the total mass penetrated by the beam, such as due to a dense tumor, will depend on the level of statistical fluctuations of the transmission through the uniform object. The statistical fluctuations of the transmission (δT) can be converted to an effective mass resolution (δX) by the expression

$$\delta X = \delta T \left|\frac{dT}{dX}\right|^{-1} \approx \sqrt{\frac{T}{N}} \left|\frac{dT}{dX}\right|^{-1}$$

or

$$(\delta X)^2 N \approx T \left|\frac{dT}{dX}\right|^{-2} \qquad (1)$$

where N is the incident beam fluence. From this expression, it is clear that the particle fluence necessary to maintain a constant δX decreases as the square of the increase of the slope of the transmission curve. For the example in Fig. 1, the ratio of the right side of Eq. (1) for x-ray and proton transmission is about 6×10^4 for a 24 cm thick object and represents the proton fluence reduction factor for the same δX. However, the proton energy required to penetrate this object is 5000 times greater than for the x-ray beam and although the dose per particle is greater for protons, the greatly reduced particle fluence yields a net reduction of the average dose of about a factor of 12 for this example. A more detailed and complete description of the application of charged particles to imaging is beyond the scope of this article and will be presented elsewhere.[8] However, it should be pointed out that measuring only the particle transmission does not yield the maximum mass resolution for charged particles since it is the energy loss or stopping power of the tissue that provides the signal and the energy fluence rather than the particle fluence which will yield the maximum information.

Method

In order to study further the advantages of proton radiography, a 205 MeV beam of protons was obtained[9] from the Booster I synchrotron at Argonne National Laboratory. Figure 2 shows a schematic diagram of the beam line used for this experiment. The proton beam which passed through

a hole in a previous target (used to produce a pulsed slow neutron beam) was directed onto a scattering foil which provided sufficient divergence to allow four 1 mm x 1 mm pencil beams to be defined by collimators just ahead of the specimen box. Each beam was separated vertically by 6.35 cm. The 23 cm water box which held the object to be radiographed was stepped horizontally across the beam at the rate of 1 mm per accelerator pulse (15 pulses/sec). At the end of each horizontal scan, the box was lowered 1 mm and the scan repeated in the opposite direction. Since the beam pulse from the accelerator was only 0.1 μsec long, individual protons could not be counted but the integrated light output from four scintillation counters placed upstream of the specimen box measured the incident flux in each beam, while four similar counters placed downstream of the specimen box measured the light output (proportional to the energy deposition) of the transmitted beam. The ratio of these two signals (relative light output) provided a measure of the total mass of material penetrated by each beam. Figure 3 shows the relationship between the measured ratio and the depth of water penetrated, a relationship which is similar to that of the well known Bragg curve.[10] The signals from each counter were recorded on magnetic tape and analyzed off-line. The total time to scan a 25 cm x 25 cm field took 18 min and was limited by the pulse rate of the accelerator. In the future with a longer pulse accelerator and a magnetically scanned beam, a scan could be completed in 0.1 sec.

The off-line analysis consisted of: (1) calculating the energy deposition ratio for each beam and scan point, (2) correcting for pulse-to-pulse energy fluctuations of the accelerator, (3) converting the ratio to a relative mass measurement using a measured calibration curve similar

to that shown in Fig. 3, and (4) displaying the relative mass data as a function of input beam position on a gray scale display unit. The gray scale on the original film was adjusted so that the resulting optical density was linearly related to the mass value for the central 150 gray levels of the total 256 level gray scale. The contrast of the display was variable, and the contrast window is indicated by a vertical gray scale tablet to the right of the displayed image, together with numbers indicating the upper and lower limits of the display window in g/cm^2, equivalent of water. The total mass of material penetrated by the beam can be obtained by adding a value of 24.7 g/cm^2 (water equivalent mass) to the displayed value, of which about 3.0 g/cm^2 is due to counters and absorber outside the specimen box. Figures 4a and 4b show the scan of a step wedge made of 0.094 g/cm^2 thick strips of lucite placed ahead of the water box. The double valued nature of the energy deposition curve is clearly evident (Fig. 4b) together with the resolution of the individual steps of the wedge. Figure 4c shows the resolution that was obtained with an x-ray beam of 120 kVp from a full wave rectified source with a total of 5.5 mm Al filtration and an FSD (film-to-source distance) of 72 in. The film used was Kodak X-omat R with a high speed calcium tungstate screen and a 10:1 grid to reduce scatter. In Fig. 4c, the steps are not directly observable although an overall change in density is observed. In Figs. 4a and 4b and all future proton radiographs, the peak back surface dose was about 45 mrad with an average dose of about 24 mrad, while the x-ray exposure in Fig. 4c had a peak front surface dose of 47 mrad.

Using the mass calibration data shown in Figs. 4a and 4b, additional absorbers were placed ahead of the downstream counters in order to ensure

a relative light output for each counter on the distal side of the peak in Fig. 3. This maintained a mass resolution as high as possible, an unique mass value, and a dynamic range of about 1.5 g/cm^2 equivalent of water. The uniform water box provided a reduction in the dynamic range required for complex specimens. However, the water box was only necessary to reduce instrumentation costs since multiple counters separated with absorber or wedge filters could have been used to expand the dynamic range to cover any fraction of the total range of the protons. The sensitivity of the proton radiographs was in fact so great that it detected a 0.008 cm nonuniformity in the water box. This nonuniformity will be detectable in some radiographs as a decreased mass in the lower lefthand corner of the box (e.g., Fig. 5b).

The increased mass resolution for a given dose can be demonstrated more directly using the phantom presented in Fig. 5, which is similar to the one developed by Burger[11] for x-ray perception studies. The phantom used here consisted of a series of air holes in mylar strips (density = 1.39 g/cm^3) which varied from 1.27 cm to 0.079 cm in diameter in five steps with the diameter doubling from one horizontal row to the next. The depth of the holes varied from 0.0127 cm to 0.813 cm in seven steps with the depth changing a factor of two from one vertical column to the next. These strips were sandwiched together between lucite blocks and the edges sealed. This phantom was placed in the 23 cm uniform water box and then scanned with the proton beam. Although the images presented here have suffered a loss of contrast and dynamic range from that of the originals, a group of five independent observers indicated that all seven holes in the 1.27 cm diameter row were detectable. This represents a mass resolution

for this size hole of 0.0127 cm of air in mylar (0.017 g/cm^2) out of a total of 24 g/cm^2 water equivalent object or 0.07%. However, detailed calculations[12] indicate that the mass resolution was not limited by the quantum noise in the proton beam, but rather by the instrumentation resolution and the energy spread and fluctuations of incident beam. Consequently, it should be possible to reduce the absorbed dose by a factor of at least four without reducing the mass resolution, if sufficient care is taken in providing a stable beam energy and small energy spread.

Figure 6 presents two x-ray radiographs of the same phantom in the same water box using the x-ray technique described previously. Figure 6a was taken at 120 kVp and had a peak dose of 47 mrad. However, a similar group of observers detected on the average less than four of the 1.27 cm diameter holes for a factor of $2^3 = 8$ less mass resolution at a similar dose to the proton radiographs in Fig. 5. Figure 6b was taken at 60 kVp and had a peak dose of 561 mrad while the observers detected on the average only 5.5 of the 1.27 cm diameter holes, a factor of three less mass resolution at 12 times the dose of the proton radiograph. If we assume that both the proton and x-ray systems were working at a contrast resolution limited only by the quantum fluctuations of the incident beam, we should expect a factor of about three improvement in mass resolution for equal dose or a factor of about nine dose reduction for equal mass resolution.[8] The unusually high improvement demonstrated here results more from the display system's capability of presenting to the observer all of the available mass resolution contained in the data, rather than being restricted to the optical density threshold of the human eye for the film-screen system.[13] The minimum detectable mass structures identified by a

group of five independent observers for each of the images in Figs. 5 and 6 are presented in Fig. 7. The x-ray data show the effect of the optical density threshold (for the 120 kVp exposure) which limits the mass resolution of the film-screen technique. The proton data show that the detection of the mass structures is well described by a constant signal-to-noise ratio modified by a limiting sampling aperture given by the proton beam size.[14]

Results

Figure 8 shows the proton scan of an excised left breast placed in a 4 in. water box and the beam energy lowered to 147 MeV. The nipple is located in the lower righthand corner, and the axillary flap extends to the left and includes some of the more dense pectoral muscle as well as some steel surgical clips in the upper left corner. The site of the original biopsy was in the lower central region and contained no residual carcinoma. The biopsy region is shown as an increased density in this region due to the higher density water compared to the surrounding lower density fatty breast tissue. At the central lefthand side of the image, a nodular structure of higher density than the surrounding breast tissue is observed. The pathology report indicated that several of the lowest axillary nodes were "grossly replaced by firm neoplastic tissue ranging in size from 0.4 to 2.5 cm in diameter" and agreed with the locations seen in the radiographs. Figure 9 presents an x-ray radiograph of the same breast in the same water box using a conventional low dose mammographic technique.[15] As a result of the 4 in. water box, the front surface dose from this technique was higher than usual and was estimated to be about 4 rad. The same structures seen in the proton radiograph (45 mrad) are

also seen in the mammograph (except for the air bubble in the center of Fig. 8) but with improved spatial resolution at the expense of a factor of 90 more absorbed dose. The spatial resolution of the proton radiograph was limited partly by the 1 mm beam size and partly by the effects of multiple scattering of the beam.

Figure 10 shows a proton radiograph of an excised human heart placed in the 23 cm water box and scanned at 205 MeV. The heart is approximately in the anatomically correct position for an anterior view of the chest. Clear separation of the right and left (more dense) ventricles is observed together with the atrioventricular groove, the auricle of the left atrium, the pulmonary trunk and the aorta. Also clearly noted is the less dense epicardial layer of the heart. Although this image of the heart was taken without the overlying skeletal structure of the chest, that structure will have less contrast in the proton radiograph than for an x-ray image. This is due to the fact that proton stopping power is essentially proportional to the electron density, rather than having the rapid Z dependence of an x-ray beam. Figure 11 shows a proton radiograph of a second heart which contained a ball and cage type artificial valve. Once again, the increased density of the left ventricle is readily observed. In Fig. 12, two thick (≈ 2.3 cm) slices of the heart shown in Fig. 11 were scanned with the proton beam and indicate a difference in the total stopping power between the left and right ventricle of the heart of about 0.1 g/cm^2 equivalent of water. This indicates a relative linear stopping power difference of approximately 0.04 between the left and right ventricular walls and should provide an easily detected signal for future charged particle imaging applications.

The relative linear stopping power for the tissue of the wall of the left ventricle was measured on the average to be 1.07 (relative to water) compared with 1.03 for the right ventricle. Since the linear stopping power is approximately proportional to the electron density of the material,[8] the relative linear stopping power should be approximately equal to the specific gravity. The values measured here are in excellent argument with the specific gravity for heart tissue of 1.04 found by Rao and Gregg.[16]

Discussion

We have demonstrated that for several biological tissues there is sufficient stopping power difference between tumor and normal tissue or between normal anatomical tissues to make proton radiography appear to have an important potential for soft tissue imaging. In addition, we have demonstrated that a significant dose reduction can be achieved with a proton radiographic system. However, the comparison between even the accelerator noise dominated proton radiographs shown here and state-of-the-art film-screen images indicates a much higher than expected improvement factor due primarily to limitations of the film-screen system.

So far no mention has been made of the effect multiple scattering will have on the spatial resolution which could be achieved in proton radiography. This property of charged particles has been of considerable concern since unlike the unsharpness (due to focal spot size or screen-film granularity) in x-ray procedures which can be improved with technical developments, the multiple scattering of charged particles is a physical property of the particles passing through matter. This will impose an ultimate limit on the attainable spatial resolution and will depend only on the type of particle, its energy, and the material. A detailed discussion of the physical

principles governing the resolution is beyond the scope of this paper and will be discussed elsewhere.[8] Briefly, as charged particles of accurately known incident position and direction pass through matter, they undergo small angle scatters. The net result of this scattering is to introduce an uncertainty in the actual trajectory of the particles and a spatial averaging of the measured stopping power over the beam spatial distribution. This spatial averaging can be expressed as a point spread function (PSF) for charged particles which is axially symmetric about the incident beam direction and decreases exponentially with r^2, where r is the radial displacement from the unscattered beam position at a given depth. The exponential coefficient (characteristic radius of the beam) of the PSF for protons is given approximately[8] by

$$r_e = \langle r^2 \rangle^{1/2} = 0.259\ R^{0.942} \left(\frac{X}{R}\right)^{3/2} \text{ mm}$$

where R = the proton range in tissue (g/cm^2)

X = depth of tissue penetrated (g/cm^2).

Figure 13 presents r_e for 200 MeV (R = 25.5 g/cm^2) protons as a function of depth in tissue, assuming that the beam position and angle incident on the front surface of the object being radiographed are known with zero uncertainty. It is obvious that the spatial averaging (blurring) will be over distances greater than 1 cm for structures near the back surface of the object. However, the charged particle spatial position can also be measured at the back surface of the object, the PSF for which will also be exponential in r^2, with an exponential slope r_e', also given in Fig. 13. In calculating r_e' (see ref. 8), it was assumed that the incident beam was uniform in intensity and normally incident on the front surface of the object. The value of r_e' is seen to increase very rapidly as a function of

distance from the back surface detector. Film can also be used as a back surface detector which combines the position and energy transmission into a single system. However, the film must always be located at the end of range of the particles and will suffer an even larger spatial averaging (blurring) than the back surface detector system, as shown in Fig. 13. From Fig. 13, it is clear that a front surface position detector or finely collimated beam as used here will result in reduced blurring over a greater depth of the object.

The variation of the blurring as a function of depth in the tissue is similar to the technique of conventional tomography or laminography, except that the focal plane is always close to the position detector. Since the position of the particles can be determined at both the front and back surface of the object, an obvious question is whether a coincident measurement of the front and rear position on a particle by particle basis could reduce the blurring function significantly. Figure 14 presents the average value and rms deviation about the average for all protons (200 MeV) with a known angle and position incident on a 24 cm object and passing through detector elements 0 to 1 mm (20% of exiting beam) or 4 to 5 mm (11% of exiting beam) away from the undeviated beam position, for detector elements placed 1 cm away from the exit surface of the object. For the example in Fig. 14, the average trajectory is well described by a quadratic function of the depth and has a maximum uncertainty of about 0.8 mm, which should be the limiting spatial accuracy that can easily be achieved with protons without the use of sophisticated deconvolution techniques. Unfortunately, the curved averaged trajectories are not easily applied in simple projection radiographic techniques but could be applied to computerized

tomographic reconstructions. Recently, tomographic reconstructions using protons have been obtained[17] which show a factor of 2 to 2.5 larger spatial resolution than for a commercial x-ray CT scanner. However, the proton tomograms were reconstructed using straight line trajectories and algorithms generated for x-ray CT data, and a significant improvement is expected if special algorithms are generated for the curved trajectories indicated in Fig. 14. Additional improvement of the spatial resolution by a factor of two or more can be obtained from using helium ions instead of protons or by using heavier ions but with some loss of the mass resolution for a given dose.

Conclusions

We have demonstrated that proton radiography does have a significant and demonstratable improvement in mass resolution for a given dose or conversely a dose reduction for a given mass resolution over x-ray techniques. In addition, the serious blurring due to multiple scattering can be reduced if coincident position information is obtained and applied to tomographic reconstruction techniques. However, a major justification for the further study of charged particle radiography may be more related to the impact it could have on complementing the information obtained from x-ray techniques and in providing a new perspective toward better understanding imaging techniques in general. Although the x-ray source (a low voltage electron accelerator) is simple in construction and operation, it produces a very complex beam which even after 80 years of use still has a very active research program on evaluating its dose effectiveness. On the contrary, particle accelerators are more complex but produce a very simple

beam which could yield a new perspective on the question of dose effectiveness of imaging modalities.

Acknowledgments

We gratefully acknowledge the assistance of Drs. E. W. Hoffman and E. F. Parker and R. C. Timm, A. T. Passi, M. J. Knott, and R. L. Stockley, and all the operating personnel of the Accelerator Research Facilities Division for providing the beam and instrumentation to make this research possible. We also would like to express our thanks to Drs. L. Skaggs, A. G. Haus, M. Rozenfeld, and R. Schlenker for their support and assistance with the x-ray comparison data.

References

1. C. A. Tobias et al., "Biomedical Studies with Heavy Ion Beams," UCRL-17357, p. 108 (1967).
2. A. M. Koehler, "Proton Radiography," Science 160, p. 303 (1968).
3. E. V. Benton et al., "Heavy Particle Radiography," Science 182, p. 474 (1973).
4. V. W. Steward and A. M. Koehler, "Proton Beam Radiography in Tumor Detection," Science 179, p. 913 (1973).
5. K. M. Crowe et al., "Axial Scanning with 900 MeV Alpha Particles," IEEE Transactions on Nuclear Science NS-23, p. 577 (1976).
6. V. W. Steward, "Proton Radiography in Medical Diagnosis," IEEE Transactions on Nuclear Science NS-22, p. 1752 (1975).
7. R. L. Martin et al., "The Proton Diagnostic Accelerator," IEEE Transactions on Nuclear Science NS-22, p. 1802 (1975). R. L. Martin, "An Accelerator for Proton Radiography," Proceedings of the IV All Union

National Conference on Particle Accelerators, Moscow, USSR, p. 370 (1975).

8. S. L. Kramer et al., "Charged Particle Radiography," to be submitted for publication.

9. D. R. Moffett et al., "Initial Test of a Proton Radiography System," IEEE Transactions on Nuclear Science NS-22, p. 1749 (1975).

10. H. Bichsel, "Charged Particle Interactions," Radiation Dosimetry, edited by F. H. Attix and W. C. Roesch, Academic Press, New York, I, p. 157 (1968).

11. G. C. E. Burger, "Phantom Tests with X-Rays," Phillips Technical Review 11, p. 291 (1950).

12. S. L. Kramer et al., "Proton Radiography," to be submitted for publication.

13. J. W. Motz and M. Danos, "Image Information Content and Patient Exposure," Medical Physics 5, p. 8 (1978).

14. R. F. Wagner, "Toward a Unified View of Radiological Imaging Systems," Part II, Medical Physics 4, p. 279 (1977).

15. A. G. Haus et al., "The Effect of Geometric and Recording Unsharpness in Mammography," Invest. Radiol. 10, p. 43 (1975).

16. P. S. Rao and E. C. Gregg, "Attenuation of Monoenergetic Gamma Rays in Tissues," Am. J. Roentgenol. 123, p. 631 (1975).

17. K. M. Hanson et al., "The Application of Protons to Computed Tomography," IEEE Transactions on Nuclear Science NS-25, p. 657 (1978).
K. M. Hanson, "Proton Computed Tomography," to be published in Proceedings of the International Federation of Information Processing Conference, Haifa, Israel, August 1978.

Figure Captions

1. Calculated transmission curves for 200 MeV protons and 40 keV x-rays in water.
2. Schematic diagram of the beam line used to provide 205 MeV protons for the radiographic data presented here. The proton beam provided by the Argonne National Laboratory Booster I synchrotron is incident from the left after passing through a hole in a previous target.
3. The ratio of the light output in the downstream counter to that in the upstream counter as a function of the total mass of water between the counters, for the 205 MeV proton beam.
4. A proton scan of the lucite step wedge described in the text. The step wedge was placed ahead of the 23 cm uniform water box and scanned with the 205 MeV proton beam. The two radiographs shown here have different contrast windows, indicated by the gray scale tablet on the right, with (a) 0.79 to 2.30 g/cm^2 and (b) 0.79 to 1.55 g/cm^2 equivalent of water. The peak back surface dose to the water box was about 45 mrad. (c) An x-ray radiograph of the same step wedge and water box taken at 120 kVp and with a peak front surface dose of 47 mrad.
5. A proton radiograph of the mass resolution phantom described in the text with contrast window settings (a) 0.743 to 2.482 g/cm^2 and (b) 1.7 to 1.9 g/cm^2. The peak dose was about 45 mrad.
6. X-ray radiograph of the mass resolution phantom shown in Fig. 5 taken at (a) 120 kVp (47 mrad peak dose) and (b) 60 kVp (561 mrad peak dose).
7. The minimum detectable mass difference for the phantom shown in Figs. 5 and 6 as a function of the diameter of the structure. The solid curve

represents a constant signal-to-noise ratio for protons (shown by the dashed curve), modified by the beam sampling aperture. The dotted curve shows the constant signal-to-noise ratio for the 120 kVp x-ray data with a threshold density of 0.01.

8. Proton radiograph taken at 147 MeV, of an excised left breast with metastatic involvement of several auxilliary lymph nodes indicated by arrow (A). The other arrows indicate: (B) the nipple, (C) the site of the original biopsy and (D) the pectoral muscle with several steel surgical clips. The contrast windows are (a) 0.94 to 1.62 g/cm^2 and (b) 1.2 to 1.6 g/cm^2. The peak absorbed dose was about 45 mrad.

9. An x-ray radiograph of the same breast in the same water box as shown in Fig. 8, taken using a conventional low dose mammographic technique. The radiograph was taken in two sections and joined together photographically. The peak absorbed dose was about 4 rads and was due to the 4 in. thick water box.

10. Proton radiograph of an excised fresh human heart in an approximately correct anatomical position for an anterior view. The contrast windows are (a) 1.0 to 2.3 g/cm^2 and (b) 1.3 to 1.9 g/cm^2. The peak dose was about 45 mrad. The arrows indicate: (A) right ventricle, (B) left ventricle, (C) right atrium, (D) atrioventricular groove, (E) aorta, (F) bifurcation of trachea, (G) epicardial tissue of the heart, and (H) the pulmonary trunk.

11. Proton radiograph of a second human heart with a ball and cage type artificial valve. The contrast windows are (a) 0.8 to 1.7 g/cm^2 and (b) 1.2 to 1.7 g/cm^2. The peak dose was about 45 mrad.

12. Proton radiograph of two slices ($\approx$ 2.3 cm thick) of the heart shown in Fig. 11. The difference between the relative stopping power of

the tissue in the walls of the left and right ventricles (indicated by arrows A and B, respectively) is about 0.1 g/cm^2 equivalent of water. The contrast windows are (a) 1.4 to 1.9 g/cm^2 and (b) 1.55 to 1.93 g/cm^2.

13. The exponential coefficient (r_e) of the point spread function for 200 MeV protons in water as a function of depth. The solid curve assumes that the spatial position of the protons was measured by a front surface detector and the dashed curve assumes a back surface position detector at 24 cm. The dotted curve is for film placed at 25.4 cm.

14. The average paths (solid curves) and the rms deviations about the average (dashed curves) as a function of depth in 24 cm of water, for the coincident position measurement technique described in the text. The cases shown are for all protons with known position and direction and having a deviation of either 0 to 1 mm (20% of beam) or 4 to 5 mm (11% of beam) from the expected (unscattered) beam position at a detector placed 1 cm away from the exit surface of the water bath.

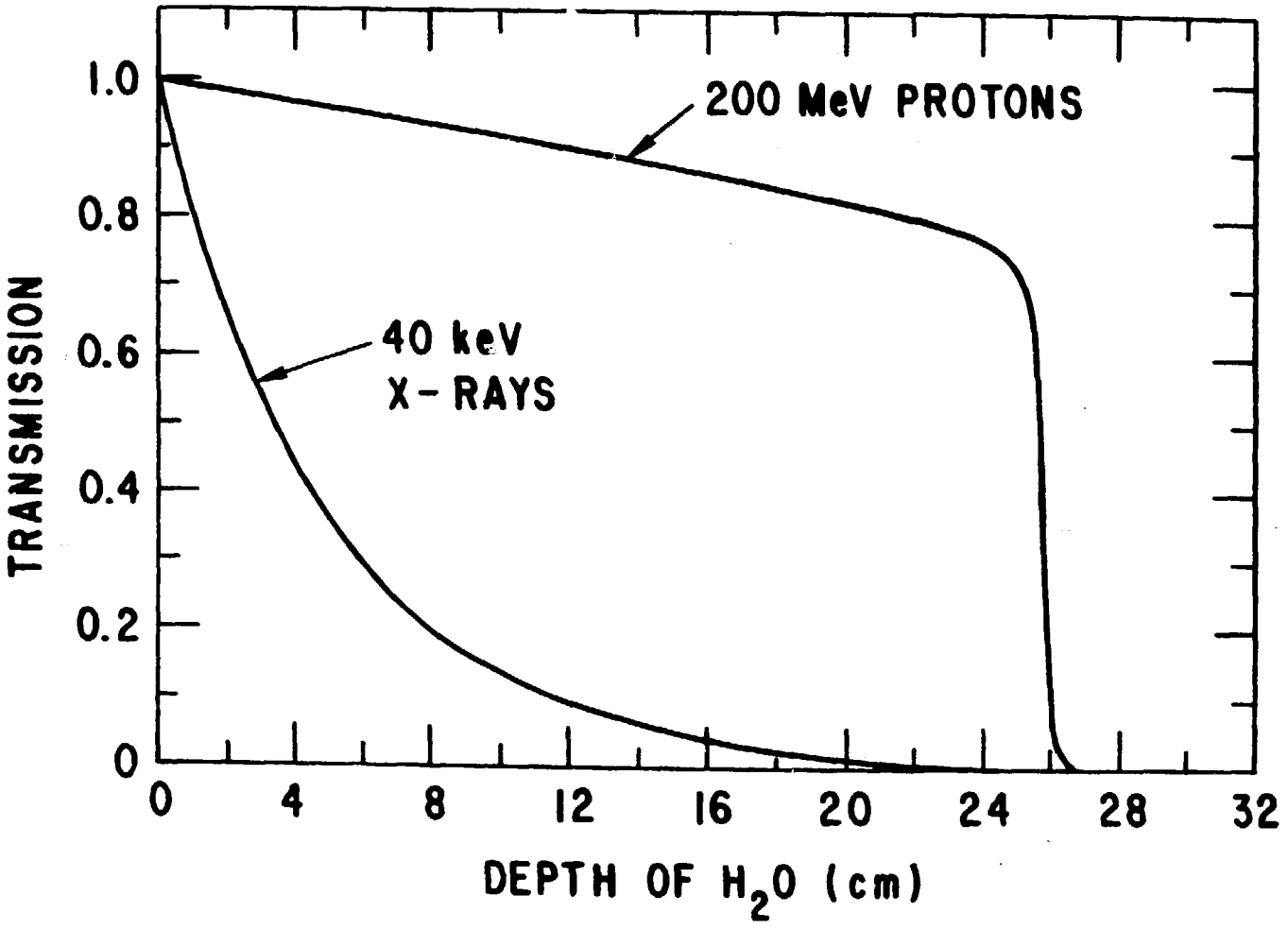
1.0
0.8
0.6
0.4
0.2
0
TRANSMISSION
200 MeV PROTONS
40 keV
X-RAYS
0
4
8
12
16
20
24
28
32
DEPTH OF H_2O (cm)

Figure 1

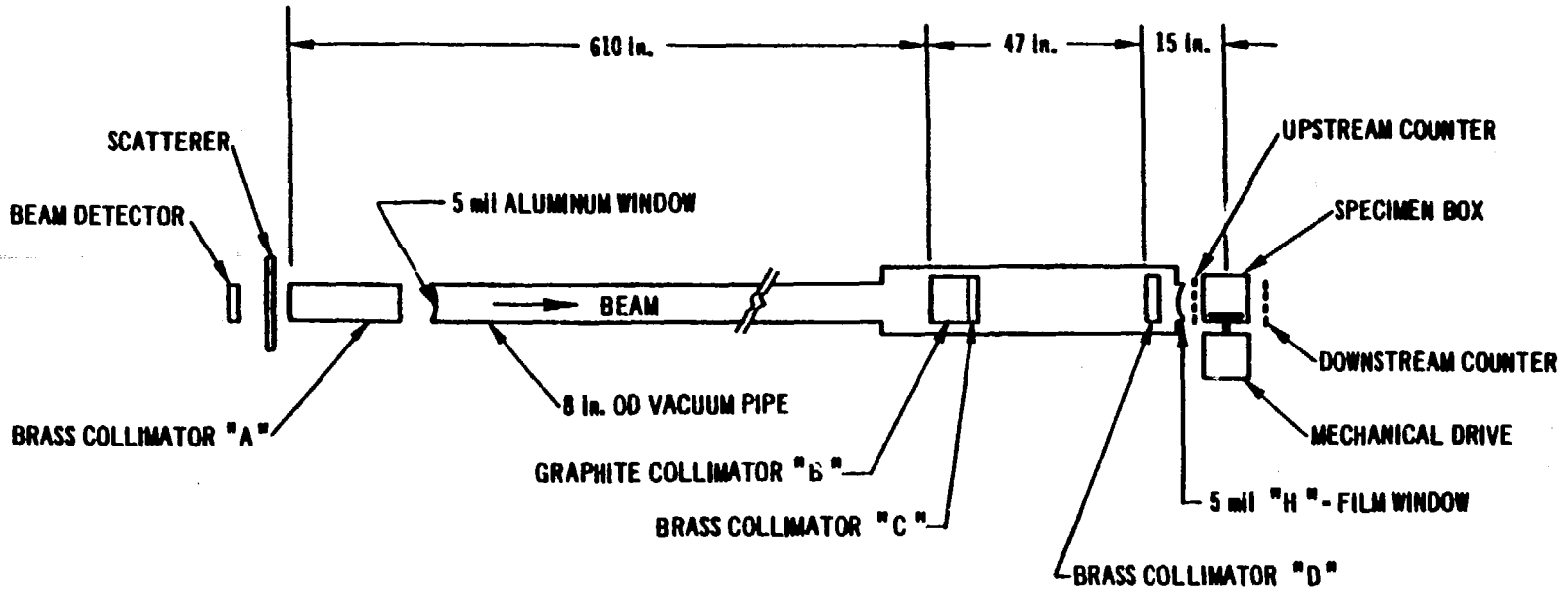
610 in.
47 in.
15 in.
SCATTERER
BEAM DETECTOR
5 mil ALUMINUM WINDOW
UPSTREAM COUNTER
SPECIMEN BOX
BEAM
DOWNSTREAM COUNTER
8 in. OD VACUUM PIPE
MECHANICAL DRIVE
BRASS COLLIMATOR "A"
GRAPHITE COLLIMATOR "B"
5 mil "H" - FILM WINDOW
BRASS COLLIMATOR "C"
BRASS COLLIMATOR "D"

Figure 2

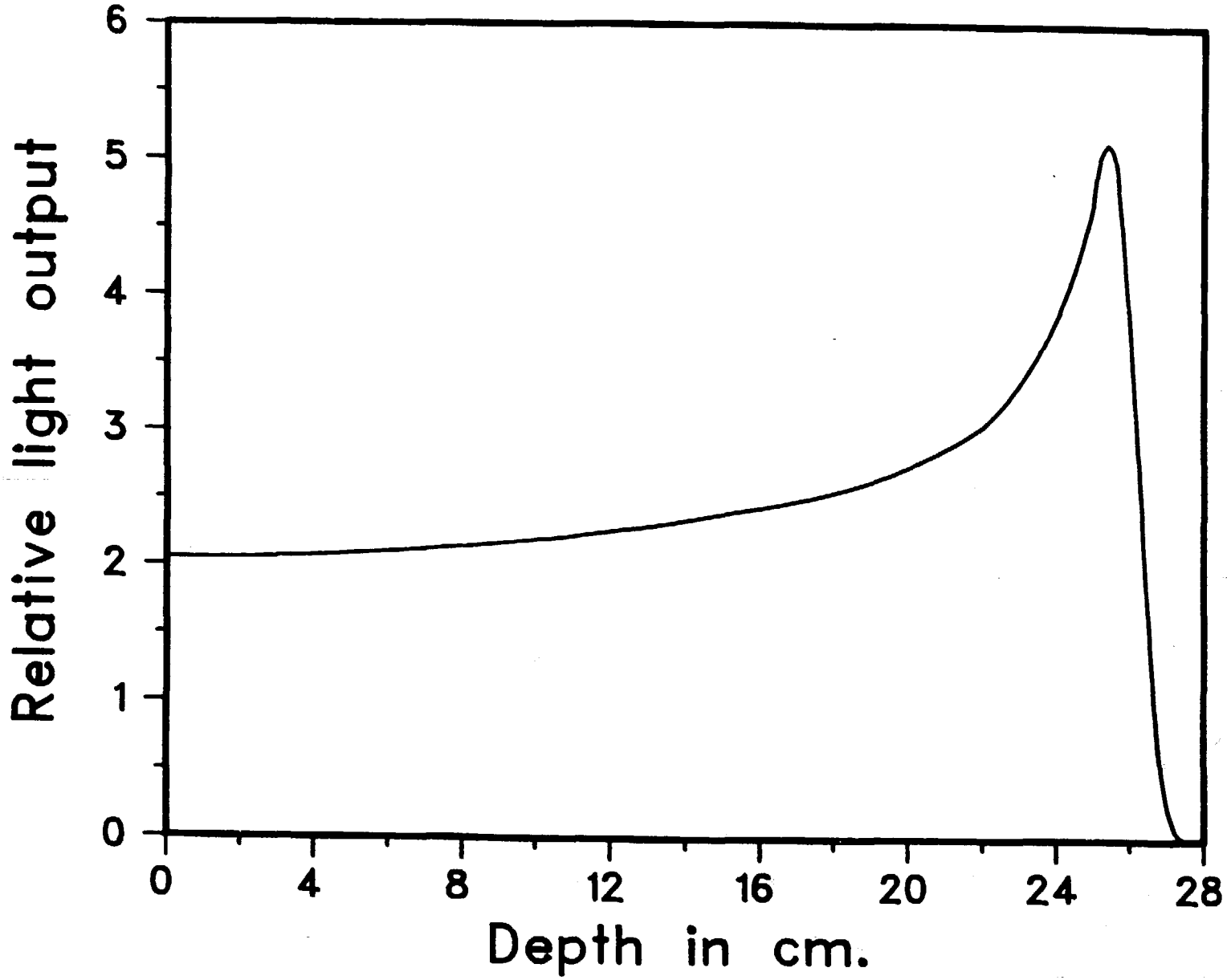

Figure 3

Figure 4a

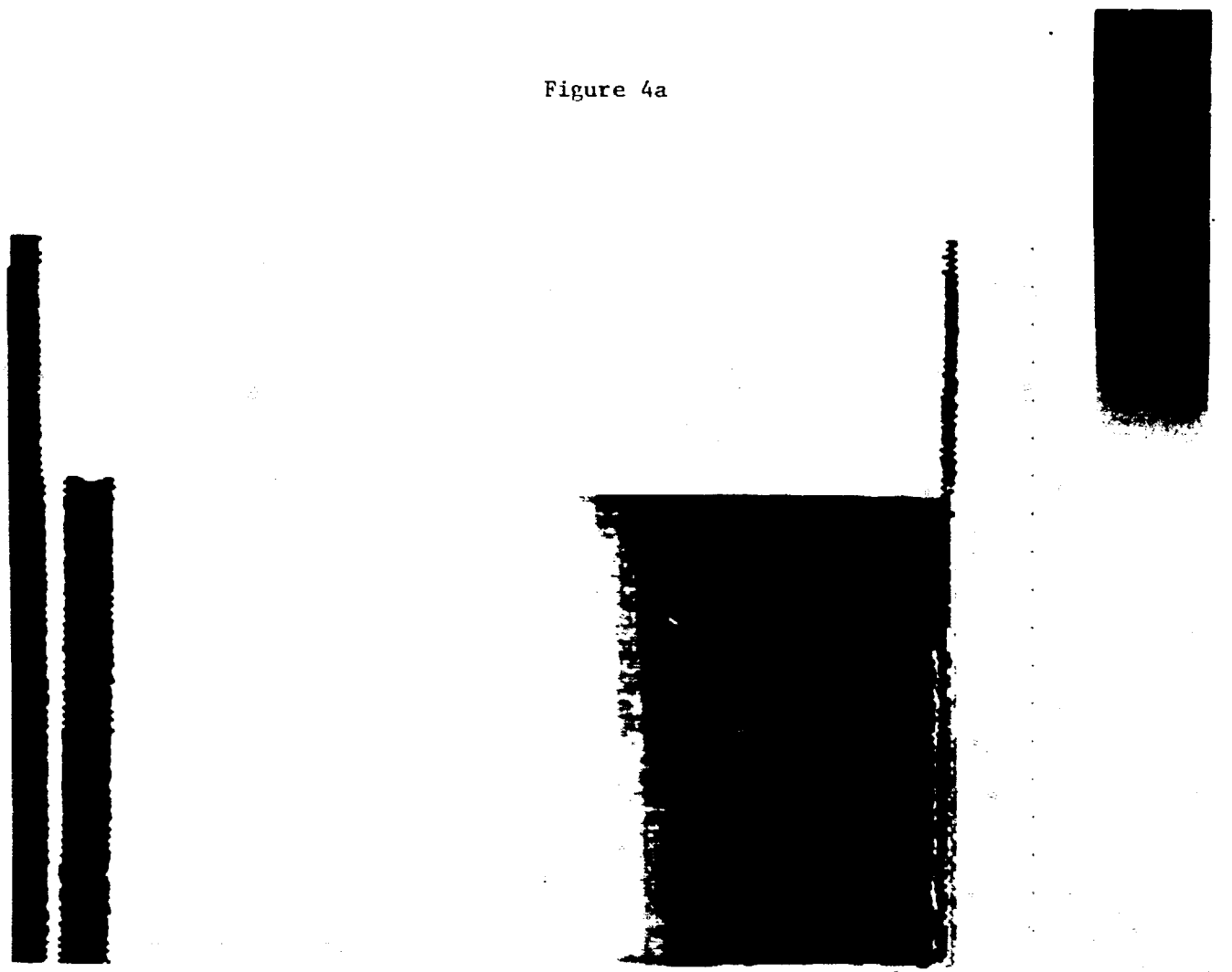

C.7938

Figure 4b

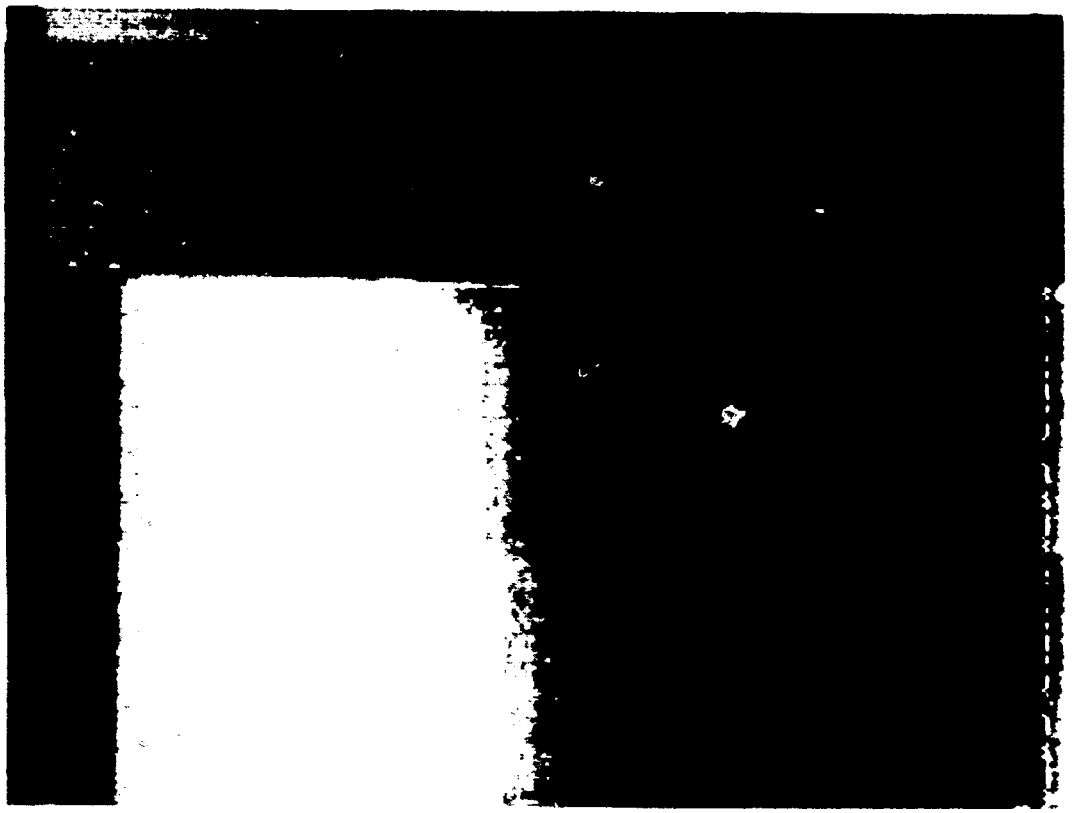

0.7938

Figure 4c

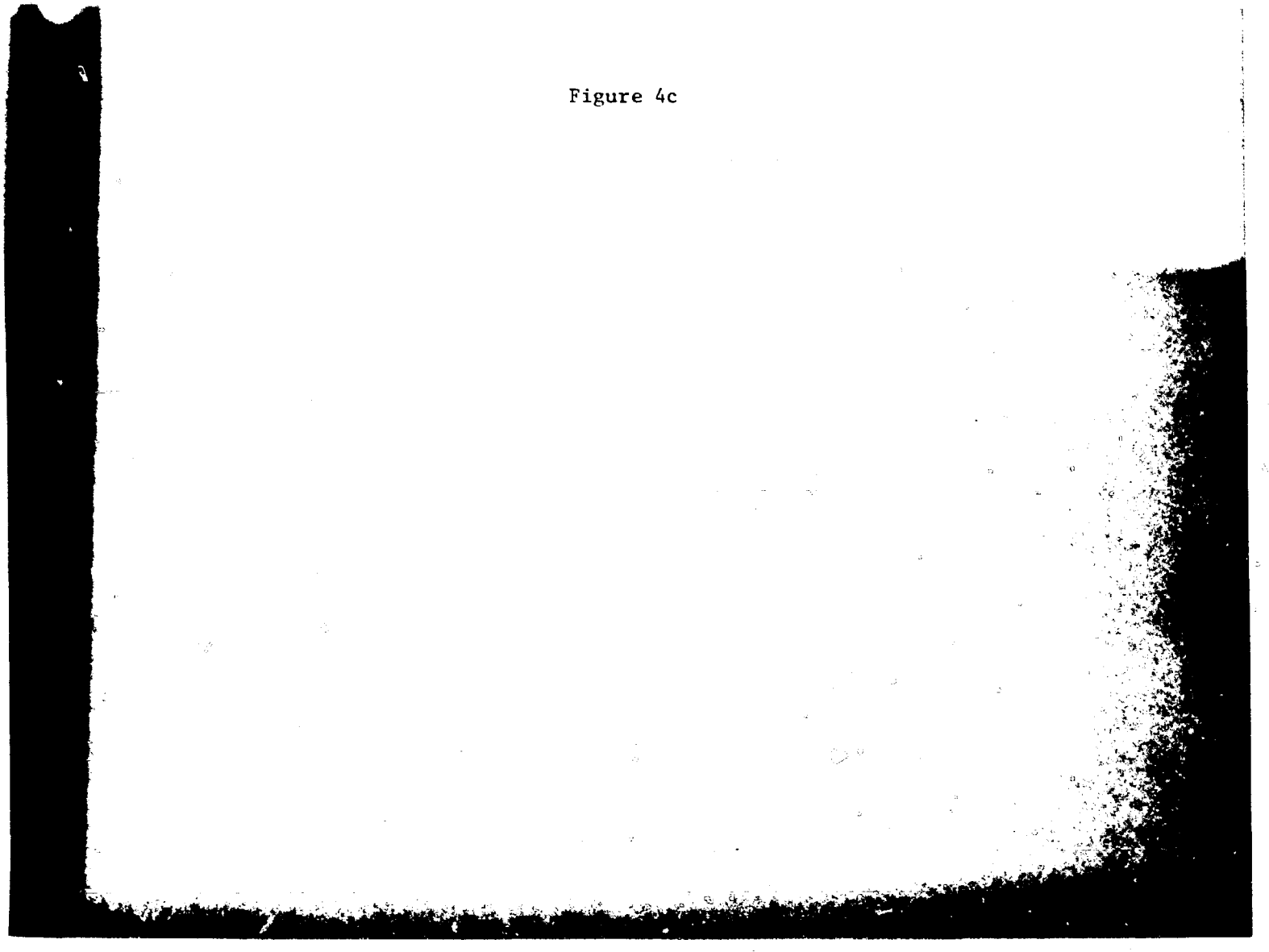

Figure 5

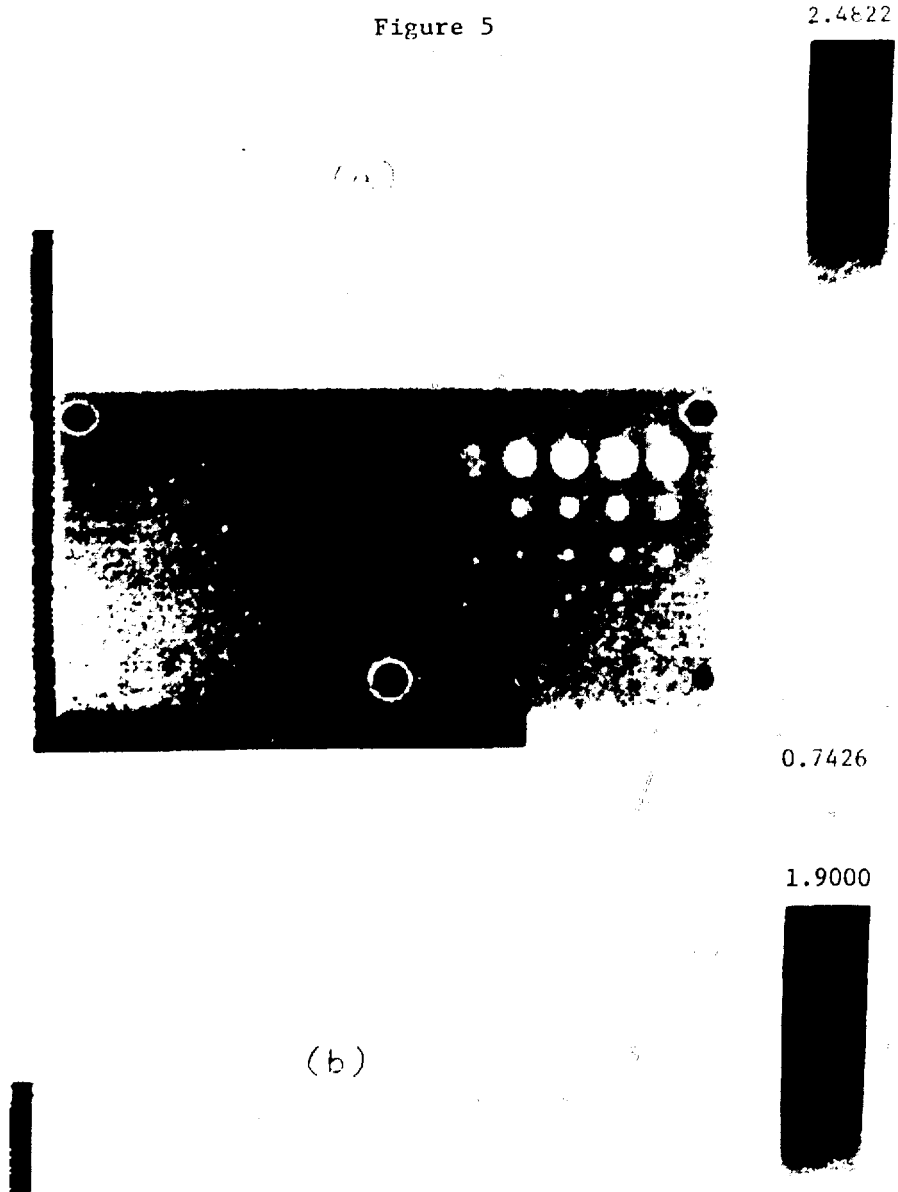

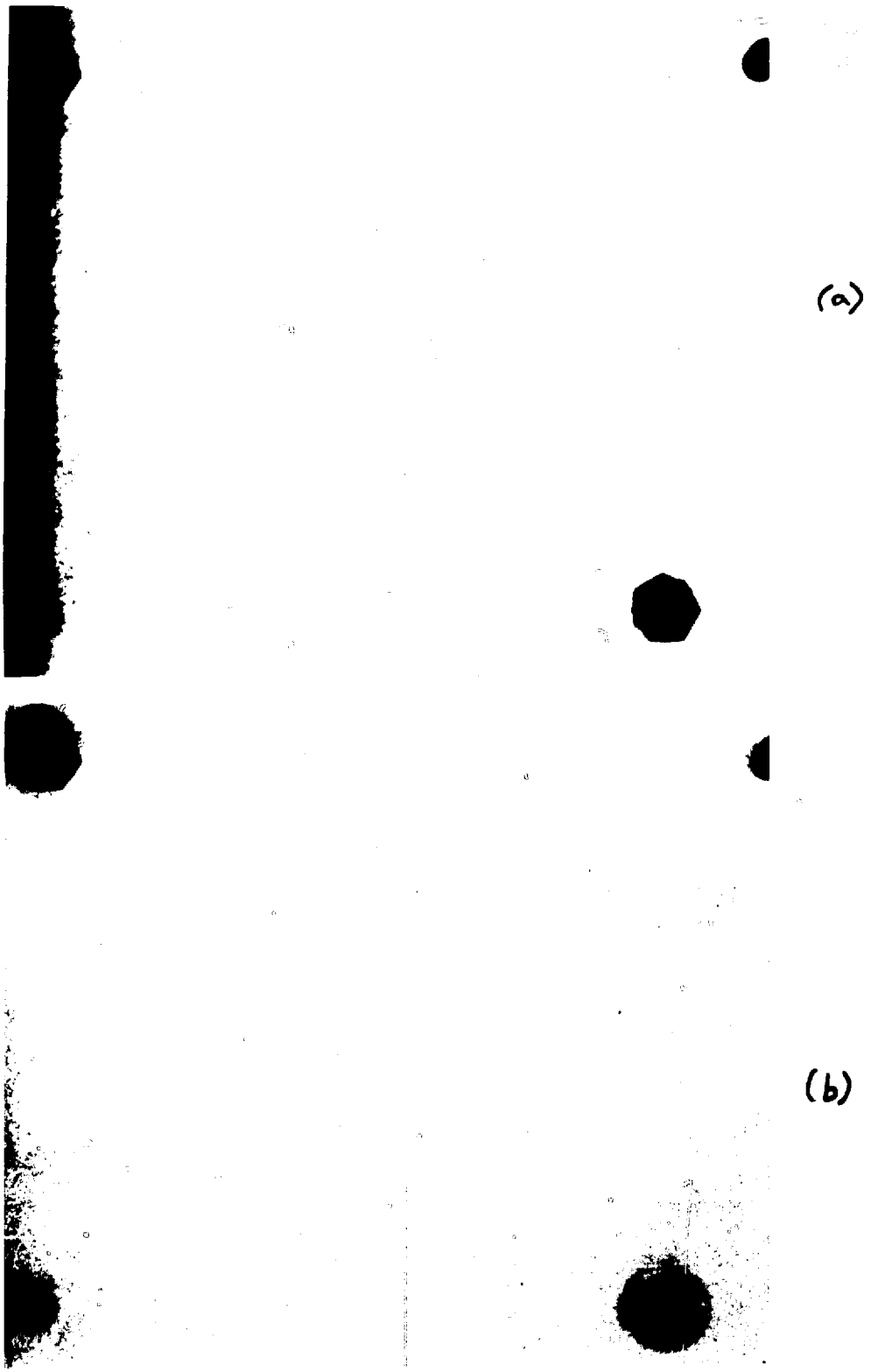

Figure 6

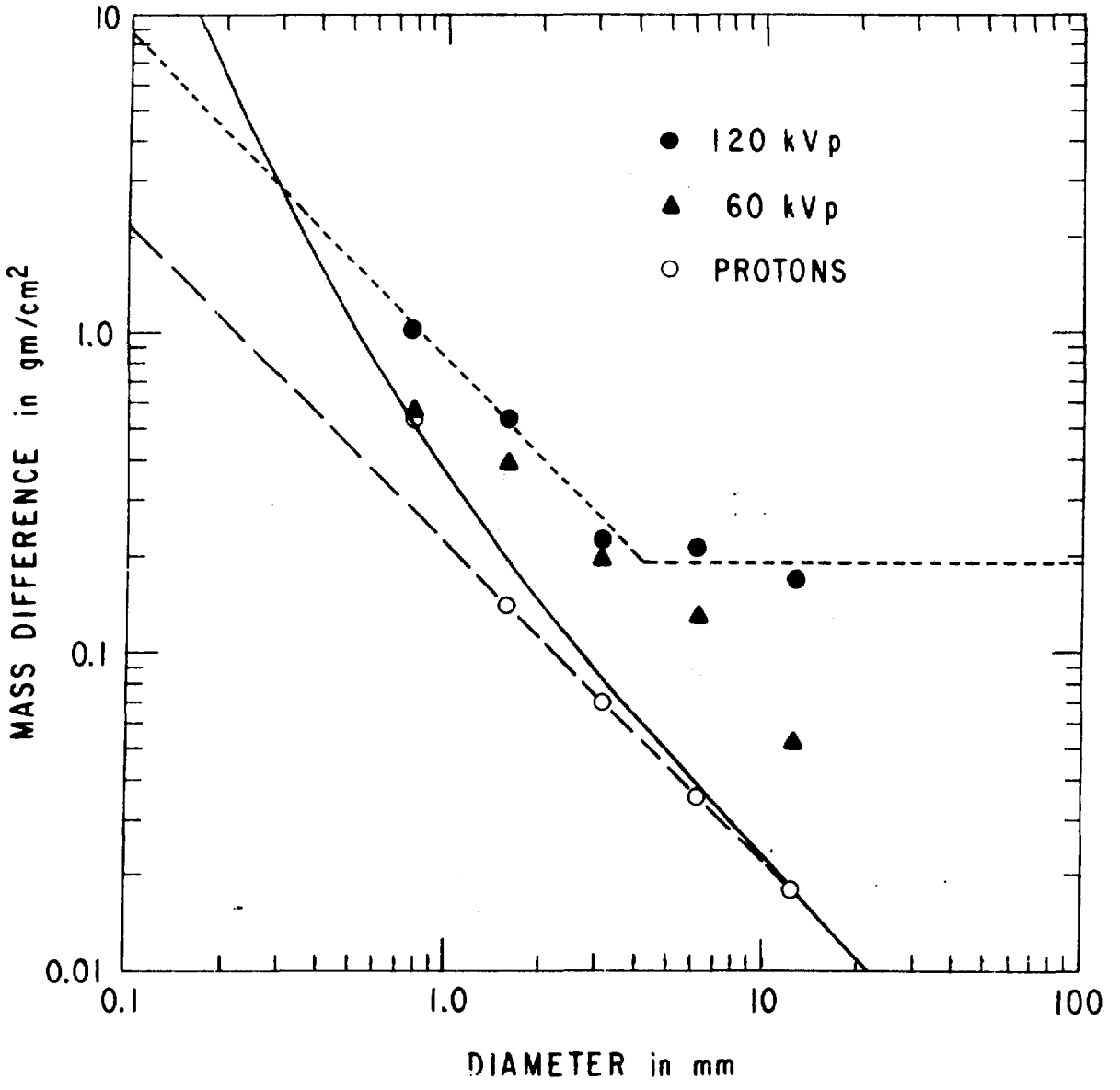
10
1.0
0.1
0.01
0.1
1.0
10
100
MASS DIFFERENCE in gm/cm²
DIAMETER in mm
120 kVp
60 kVp
PROTONS

Figure 7

Figure 8a

Figure 8b

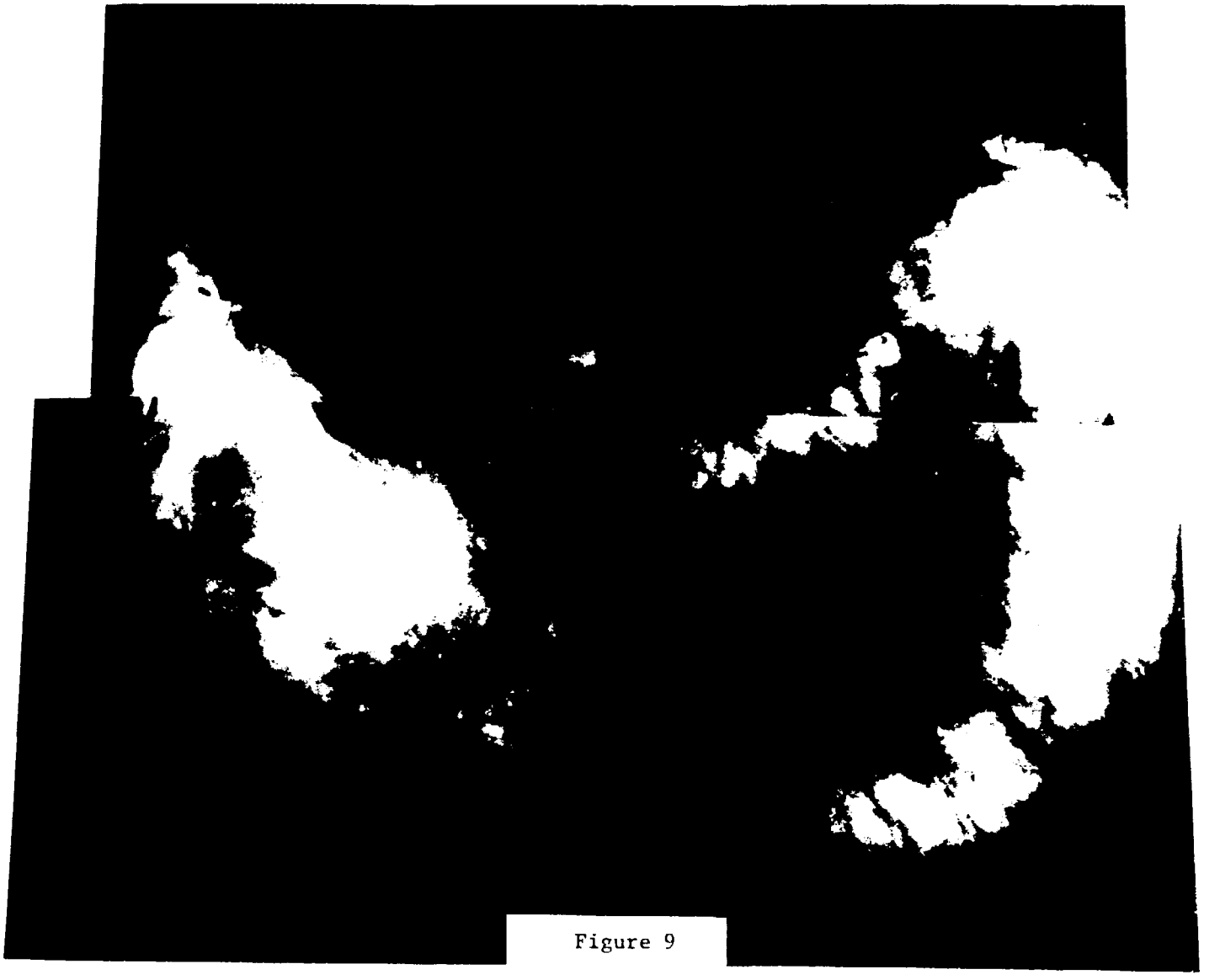

Figure 9

Figure 10a

Figure 10b

Figure 11a

Figure 11b

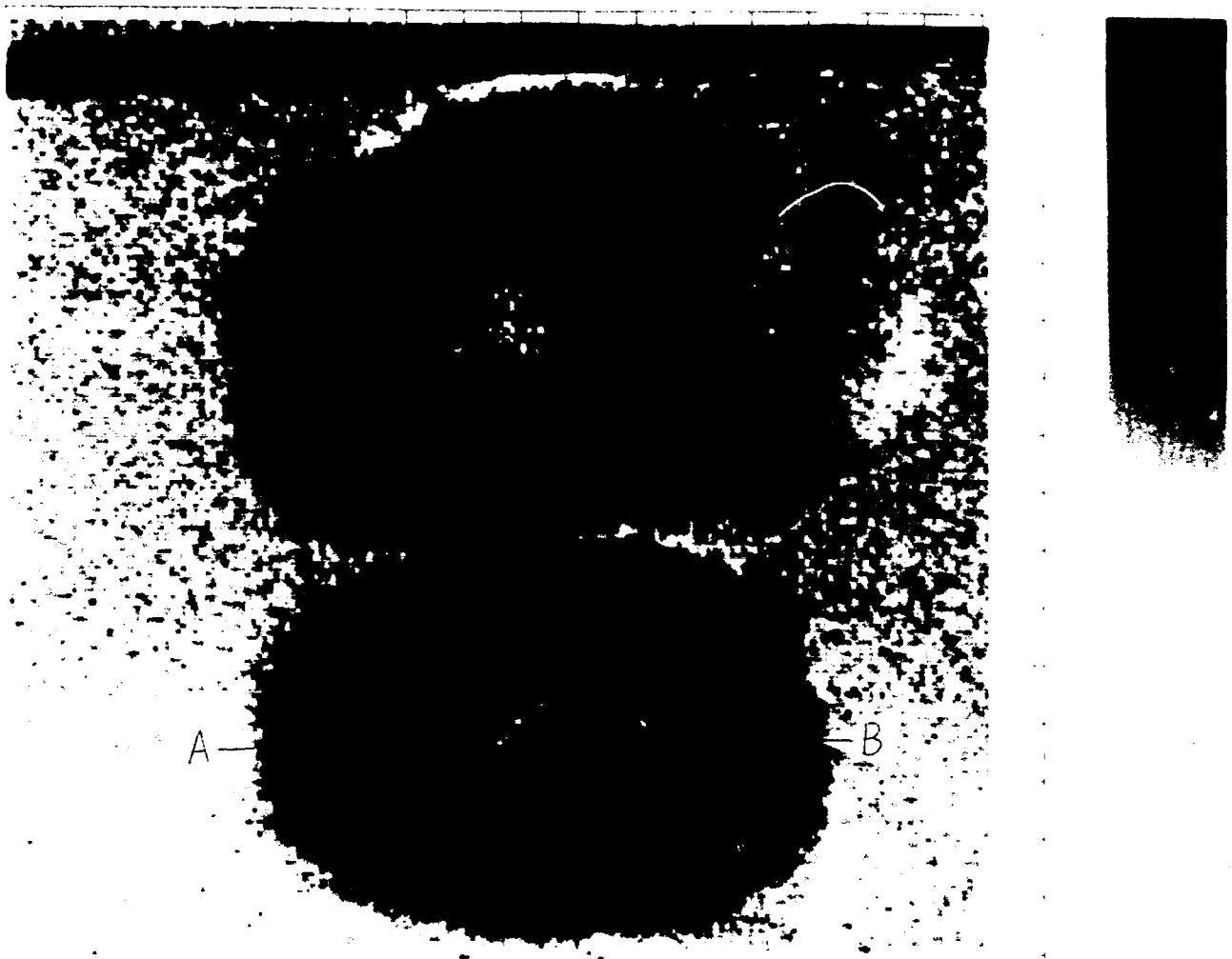

Figure 12a

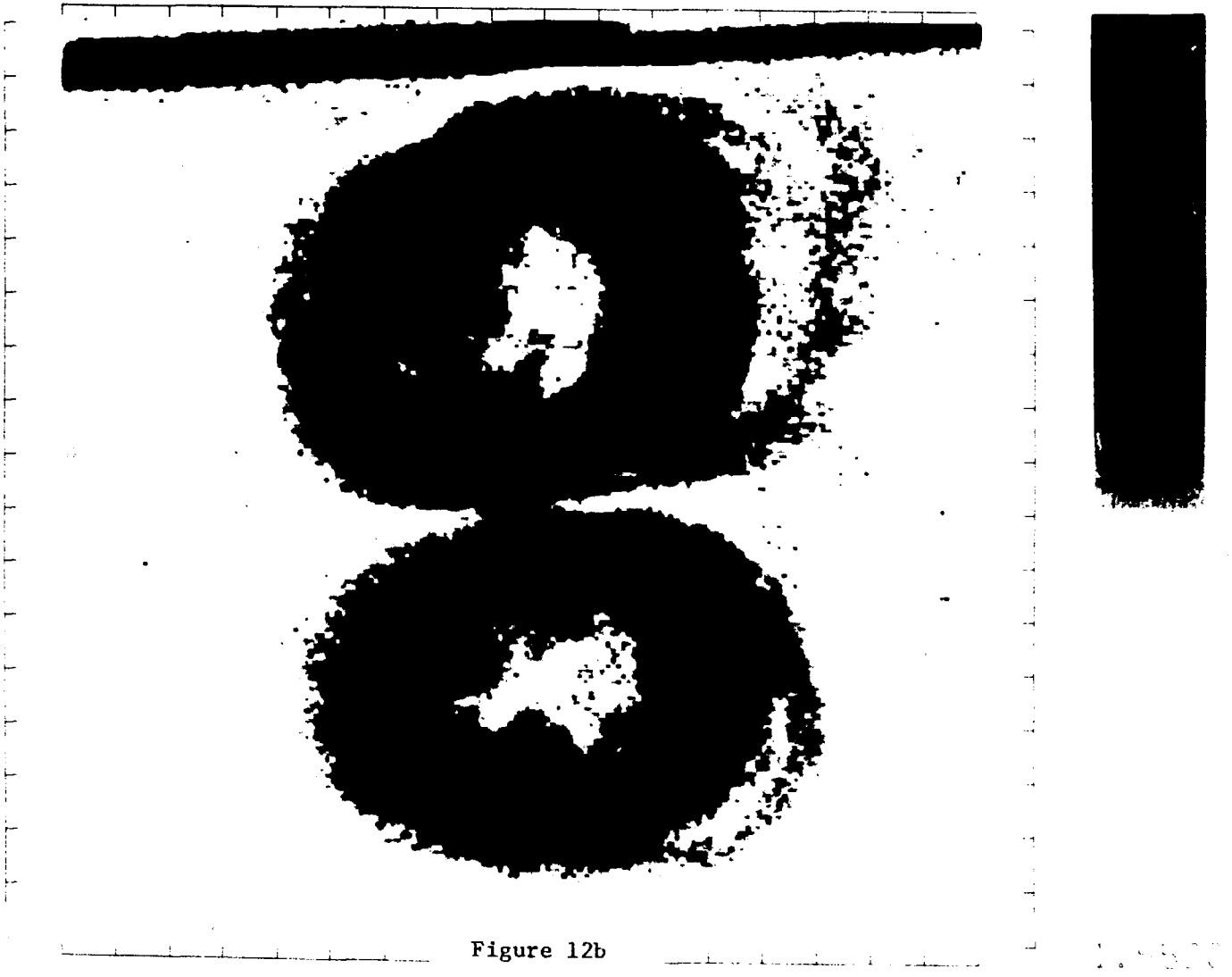

Figure 12b

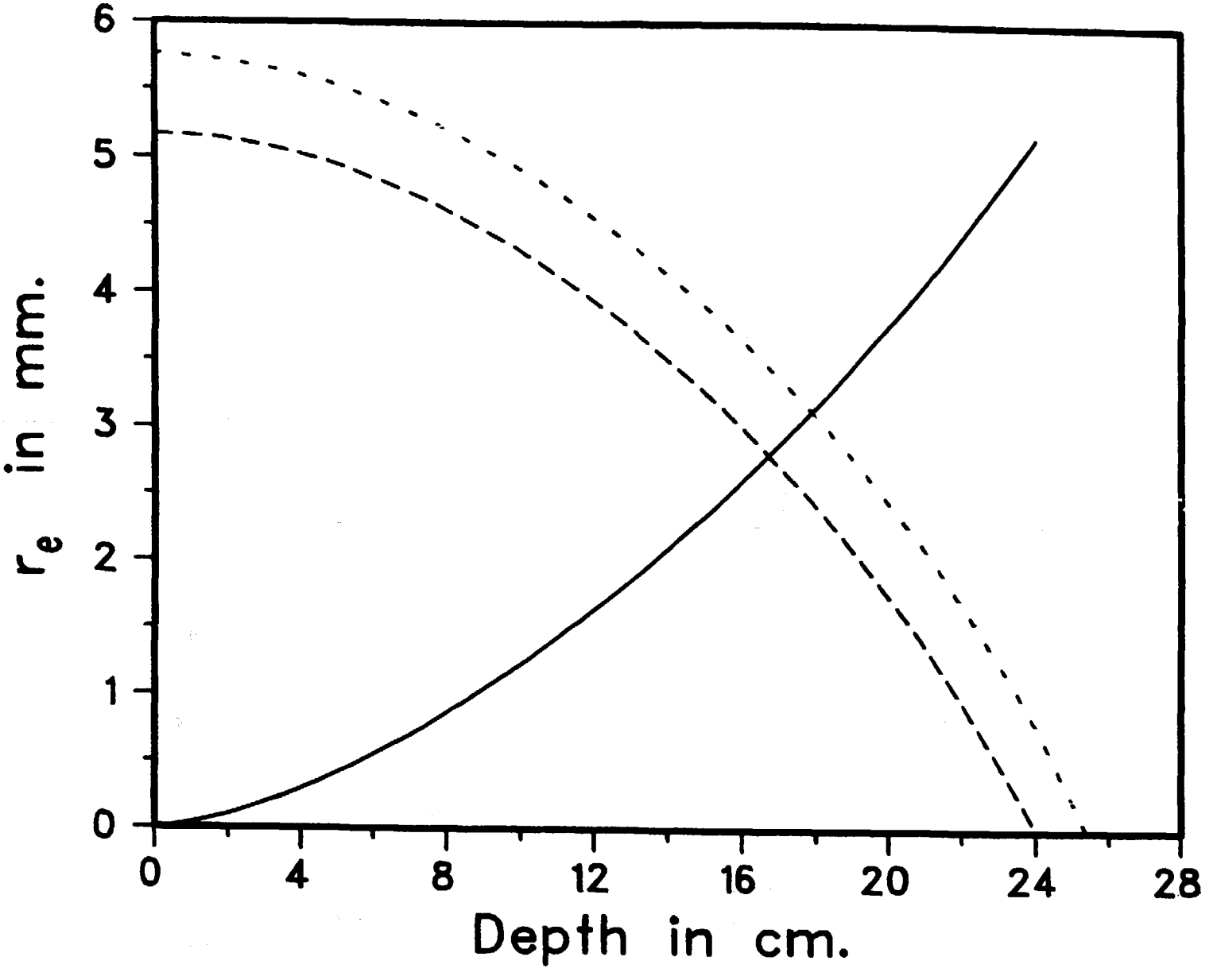

Figure 13

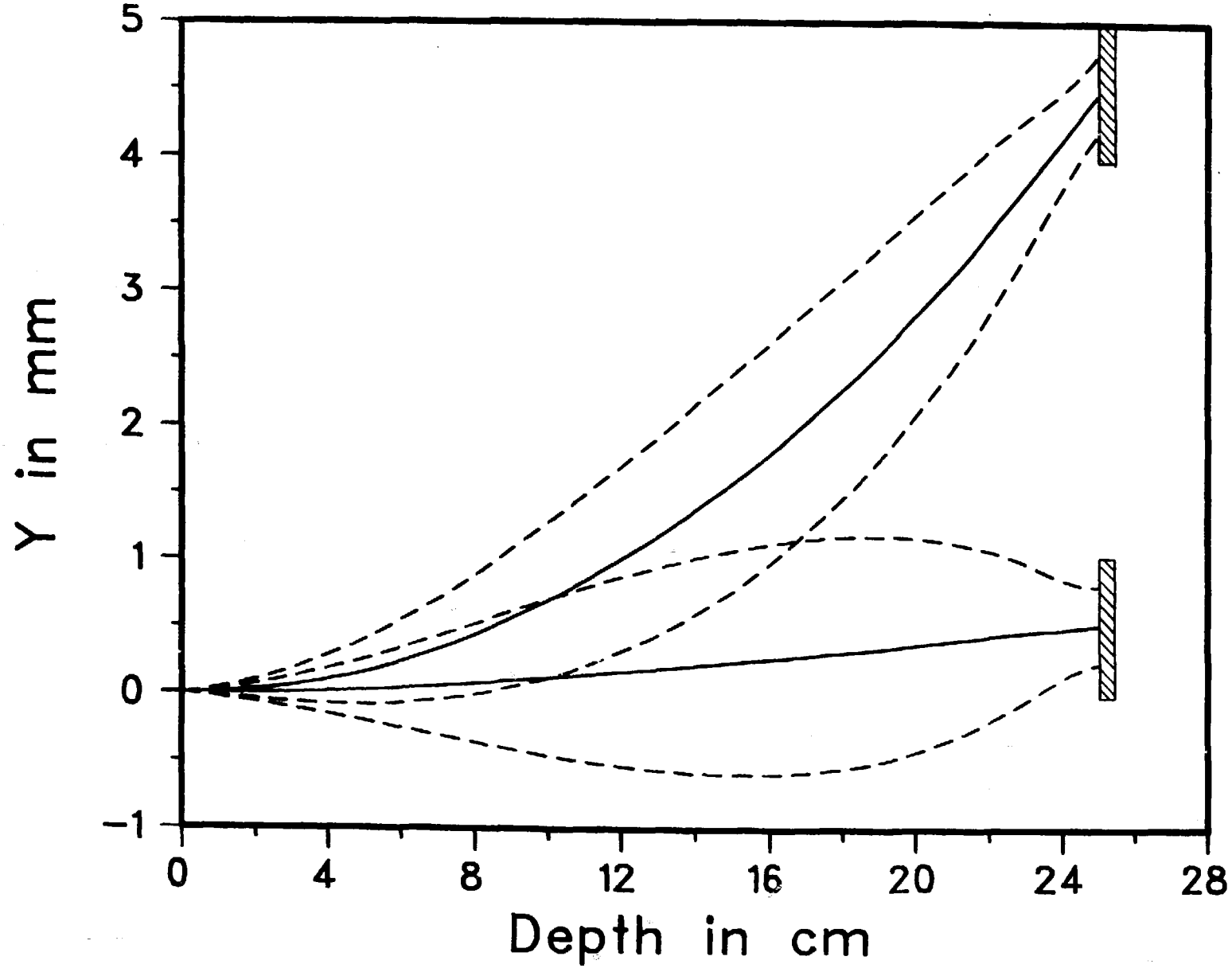

Figure 14